RESEARCH ARTICLE

Check for updates

The dual effect of "inorganic fullerene" {Mo$_{132}$} doped with SnO$_2$ for efficient perovskite-based photodetectors†

Xueying Xu,[a] Liming Zhang,*[b] Ting Wang,[a] Yunjiang Li,[a] Tuo Ji,[a] Weilin Chen, [iD] *[a] Chunlei Wang[c] and Chunxia Lin[d]

The electron transport layer (ETL) transfers the photogenerated electrons generated by the perovskite layer to the conductive glass substrate, which plays a vital role in the performance of the perovskite-based photodetector. SnO$_2$, as a wide bandgap semiconductor, is a promising ETL material, but the interface electronic recombination between it and the perovskite layer limits the improvement of device efficiency. It is hopeful that {Mo$_{132}$} will solve this problem. Here, we doped SnO$_2$ with {Mo$_{132}$}, which can simultaneously adjust the energy level of SnO$_2$ and increase the crystallinity of the perovskite crystal, thereby reducing interface electronic recombination. The conduction band of the obtained composite material moves down by 0.11 V, which is more conducive to the transfer of photogenerated carriers. Moreover, the doping of {Mo$_{132}$} significantly increases the ultraviolet light absorption intensity of the composite material, which is conducive to the collection of sunlight. In addition, the oxygen vacancy content of the composite material is reduced, which is conducive to reducing the electron recombination center. Therefore, the photocurrent of the device is increased from 13.32 µA to 27.04 µA, an increase of about 1.03 times.

1. Introduction

Organic–inorganic metal halide perovskite materials have attracted extensive attention from researchers all over the world owing to their excellent performance, and they are widely used in solar cells,[1–8] luminescent materials,[9–15] photodetectors,[16–31] photocatalysis[32–34] and other fields. The main characteristics of organic–inorganic metal halide perovskites are that they have a tunable bandgap, a higher carrier migration rate, and a better light absorption efficiency.[35–38] However, the perovskite film itself has ion migration and defect states,[39–41] and the energy level mismatch also exists between the perovskite layer and the electron transport layer (ETL).[42] These problems will lead to the

accumulation of photogenerated electrons between the perovskite layer and the ETL, and reduce the efficiency of perovskite-based devices by producing interface electron recombination.[43] TiO$_2$ has been widely used as the ETL of perovskite-based devices due to its suitable energy level, but the energy-consuming high-temperature production process of TiO$_2$ (>450 °C) limits its large-scale commercial application.[44] Moreover, the instability of TiO$_2$ under ultraviolet light will also cause the ultraviolet light decomposition of the perovskite layer.[45–47]

SnO$_2$ is a wide-bandgap n-type semiconductor with a higher electron migration rate and is expected to replace TiO$_2$ as the electron transport material (ETM).[48] SnO$_2$ has a low-temperature preparation process,[49] so it can save energy to a large extent. Besides, SnO$_2$ has good ultraviolet-visible and chemical stability, which can improve the stability of the device.[48,50,51] However, compared with the electron mobility of the perovskite layer ($0.5–30$ cm^2 V^{-1} s^{-1}), the electron mobility of n-type semiconductor SnO$_2$ (10^{-3} cm^2 V^{-1} s^{-1}) is still very low.[52,53] The interface electron recombination caused by this difference in electron mobility will greatly reduce the device efficiency. Fullerene and its derivatives are a kind of carbon material with good electrical conductivity, which have been widely used in ETM. Typically, Liu et al. used fluoroalkyl substituted fullerenes and perovskites to form a heterojunction structure.[54] This fullerene derivative realizes the effective passivation of the perovskite,

[a] Key Laboratory of Polyoxometalate and Reticular Material Chemistry of Ministry of Education, Faculty of Chemistry, Northeast Normal University, Changchun, 130024, China. E-mail: chenwl@nenu.edu.cn

[b] State Key Laboratory of Luminescence and Applications, Changchun Institute of Optics, Fine Mechanics and Physics, Chinese Academy of Sciences, Changchun 130033, China. E-mail: zhangliming@ciomp.ac.cn

[c] Library of Northeast Normal University, Changchun, 130024, China

[d] Vocational Education Center of Huadian City, Jilin Province, Huadian, 132400, China

† Electronic supplementary information (ESI) available: Additional experimental details including EDX, XPS, I–T curve, Mott–Schottky curve and O content calculation table. See DOI: 10.1039/d1qm00618e

reduces the hysteresis phenomenon, and improves the stability of the device. Fu *et al.* introduced the functional fullerene into the perovskite through the anti-solvent method, which can not only control the crystallization of the perovskite, but also passivate the surface defects of the perovskite, thereby improving the performance of the device.[55] Additionally, the thickness of the thin SnO_2 layer prepared by spin coating is about 30 nm, and the film has poor wettability, which will affect the quality of the perovskite layer grown on it.[51,56] The method currently studied to improve the wettability of the SnO_2 surface is doping. For example, Hui *et al.* modified SnO_2 by doping red carbon quantum dots rich in hydroxyl and carboxyl ligands to improve the performance of the device.[57] At present, studies have shown that fullerenes are a type of effective function material to reduce the interface electronic recombination of SnO_2.[58–60] However, the expensive cost and complex synthesis processes limit their wide application. Therefore, it is particularly important to find a substitute for fullerene materials.

Polyoxometalate is a kind of cluster compound composed of transition metal and oxygen, which has been widely used in photoelectric catalysis, photodetection and other fields due to the characteristics of acting as a shallow electron trap and effectively separating photogenerated excitons.[61–71] Kepler-type polyoxometalates, as an important branch of polyoxometalates, have a special wheel-like structure. Among them, $(NH_4)_{42}[Mo_{72}^{VI} Mo_{60}^{V}O_{372}(CH_3COO)_{30}(H_2O)_{72}]$ ($\{Mo_{132}\}$), as a polyoxometalate with an inorganic fullerene-like structure, is expected to become an inorganic material to replace fullerene. Its structure is shown in Fig. S1 (ESI†). $\{Mo_{132}\}$ is built up of 12 $\{Mo_{11}\}$ fragments of the type $\{(Mo)Mo_5\}\{Mo_1^{V}\}_5$ with central pentagonal bipyramidal $\{MoO_7\}$ groups, such that the fivefold symmetry axes are retained in the resulting spherical object, which shows an overall icosahedral symmetry, which includes the respective C_2 and C_3 symmetry axes. The structure of fullerene C_{60} is also composed of a pentagonal face and a hexagonal face. Its molecular point group is I_h, with five-fold symmetry, which is consistent with the structural symmetry of Mo_{132}. This spherical structure facilitates the transmission of electrons. $\{Mo_{132}\}$ has high redox activity and rapid electronic transfer capability. It has been used to modify photoanodes in dye-sensitized solar cells.[72] Besides, the suitable energy level, abundant carboxyl ligands and wide ultraviolet-visible light absorption range of $\{Mo_{132}\}$ can elevate the performance of perovskite devices by improving the crystallization of the perovskite, reducing the interface electronic recombination and improving the light absorption.

ETL has an important impact on device performance. It is necessary to simultaneously adjust the energy level and electron mobility of SnO_2 and solve the problem of growing a high-quality perovskite layer on the SnO_2 layer. In this work, we doped the SnO_2 with polyoxometalates $\{Mo_{132}\}$ containing abundant carboxyl ligands and applied it to perovskite-based photodetectors. $\{Mo_{132}\}$ is a kind of light-induced electron donor/acceptor, which not only enhances electron transport, but also adjusts the energy level of SnO_2 to make it more compatible with the perovskite layer. At the same time, the abundant carboxyl ligands on $\{Mo_{132}\}$ can passivate the grain

boundary of the perovskite layer and promote the increase of the crystallinity of the perovskite film, effectively solving the problem of uneven perovskite growth on the SnO_2 layer. Disorderly existed COO^- in Mo_{132} can coordinate with Pb^{2+} ions, delay the crystallization of PbI_2, reduce the trap state of Pb^{2+}, and realize the passivation effect of Pb^{2+}, as shown in Fig. S2 (ESI†).[73,74] The doped $SnO_2@Mo_{132}$ has significantly improved crystallinity and ultraviolet light absorption intensity, and the doped SnO_2 oxygen vacancy content is reduced. These are all beneficial to the reduction of electronic recombination of the device. Therefore, the photocurrent of the photodetector based on the composite $SnO_2@Mo_{132}$ is significantly increased by ~ 1.03 times.

2. Experimental

2.1 Synthesis of Mo_{132}

$\{Mo_{132}\}$ is synthesized according to the literature method.[75] $N_2H_4 \cdot H_2SO_4$(0.8 g, 6.1 mmol) is added to 250 mL aqueous solutions of $(NH_4)_6Mo_7O_{24} \cdot 4H_2O$ (5.6 g, 4.5 mmol) and CH_3COONH_4 (12.5 g, 162.2 mmol). The color of the solution changes from blue to green. After that, 50%(v/v) CH_3COOH (83 mL) is added to the solution. After placing the solution at room temperature for 3–4 days, red-brown $\{Mo_{132}\}$ crystals are obtained.

2.2 Preparation of $SnO_2@Mo_{132}$ precursor

A tin(IV) oxide, 15 wt% colloidal dispersion is diluted to 2.67 wt% with deionized water to obtain the SnO_2 precursor. Mo_{132} (2–5 mg mL^{-1}) is added to the SnO_2 precursor solution and stirred at room temperature for 3 h to obtain a $SnO_2@Mo_{132}$ precursor solution.

2.3 Device fabrication

A schematic diagram of the preparation procedure and device structure of the device is shown in Fig. 1. SnO_2 and $SnO_2@Mo_{132}$ precursors are spin-coated on clean ITO/glass at 3000 rpm for 30 s and then annealed at 150 °C for 30 min to obtain the electron transport layer (ETL). The perovskite precursor is prepared by dissolving 0.461 g PbI_2 and 0.157 g CH_3NH_3I (MAI)
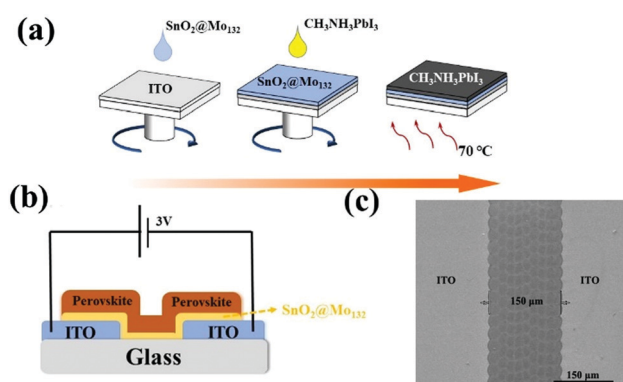

Fig. 1 (a) Schematic diagram of the procedure for preparing the device; (b) structure of the device; (c) SEM image of the ITO substrate treated with a laser pattern of perovskite films grown on SnO_2 and $SnO_2@Mo_{132}$.

in 1 mL of DMF : DMSO = 4 : 1 (v:v) solution and stirring for 12 h. The perovskite precursor solution is spin-coated on the ETL at 2000 rpm for 60 s and anneals at 70 °C for 30 min to obtain the perovskite layer. The preparation of the perovskite precursor solution, spin coating, and annealing operations are all completed in the glove box filled with N_2.

3. Results and discussion

3.1 Characterization of $SnO_2@Mo_{132}$ composite

To study whether the chemical structure of SnO_2 has changed, we analyzed the infrared spectrum (IR) and X-ray diffraction spectrum (XRD) of SnO_2 and $SnO_2@Mo_{132}$ (Fig. 2a and b). It can be seen from the IR of $\{Mo_{132}\}$ in Fig. 2a that the broad peaks in the region of 3600–3200 cm^{-1} correspond to ν(O–H), and the absorption peaks at 968 cm^{-1} and 935 cm^{-1} are attributed to the $Mo{=}O$ bond, the absorption peak at 792 cm^{-1} is attributed to the Mo–O–Mo bond, and the absorption peaks at 1546 cm^{-1} and 1404 cm^{-1} are attributed to COO^- and NH_4^+ groups, respectively, which are characteristic peaks of Kepler-type $\{Mo_{132}\}$.[76] With the doping of polyoxometalate and SnO_2, it can be seen that the absorption peak intensity of COO^- and NH_4^+ groups at 1546 cm^{-1} and 1404 cm^{-1} decreases. The absorption peak intensity of the $Mo{=}O$ bond located at 968 cm^{-1} and 935 cm^{-1} also decreased, both of which indicate the interaction between polyoxometalate and SnO_2. It can be seen from Fig. 2b that compared with the standard XRD card of SnO_2, the diffraction peaks located at 26.31°, 33.86° and 51.83° correspond to the (110), (101) and (211) crystallographic planes, respectively.[77] Fig. 2b also shows that the main diffraction peaks of the doped SnO_2 do not shift significantly but their intensity increases, indicating that doping of $\{Mo_{132}\}$ does not change the structure of SnO_2 but can increase the crystallinity of SnO_2 crystals. In addition, it is worth mentioning that no diffraction peak of $\{Mo_{132}\}$ can be observed in the XRD of the composite material, which is attributed to the low content of $\{Mo_{132}\}$.

In order to further study the composite material $SnO_2@Mo_{132}$, we performed scanning electron microscope (SEM) and transmittance electron microscope (TEM) tests on SnO_2 and $SnO_2@Mo_{132}$ to
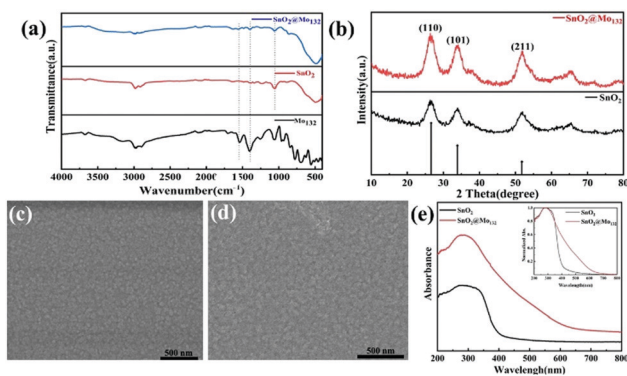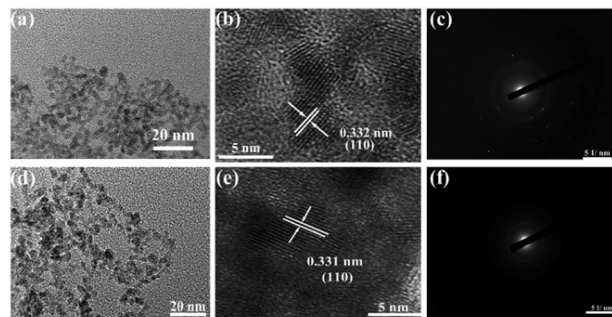
Fig. 3 (a) Transmission electron microscope image of SnO_2; (b) high resolution transmission electron microscope image of SnO_2; (c) selected area electron diffraction image of SnO_2; (d) transmission electron microscope image of $SnO_2@Mo_{132}$; (e) high resolution transmission electron microscope image of $SnO_2@Mo_{132}$; (f) selected area electron diffraction pattern of $SnO_2@Mo_{132}$.

characterize their morphology and crystallinity, as shown in Fig. 2c, d and 3. From the scanning electron micrograph, we can see that both SnO_2 and $SnO_2@Mo_{132}$ layers can uniformly cover the ITO surface, with a grain size of 5–10 nm, which is consistent with the literature.[78] Doping does not change the morphology of the SnO_2 layer. This is consistent with the result observed at 20 nm in the TEM image. Fig. 3b and e are high-resolution TEM test images of SnO_2 and $SnO_2@Mo_{132}$, respectively, and Fig. 3c and f show the corresponding electron diffraction patterns. Both can see clear lattice fringes and the lattice fringe spacings are measured to be 0.332 nm and 0.331 nm, respectively, corresponding to the (110) crystal plane of SnO_2,[79] which is consistent with the XRD test results, indicating that the SnO_2 has high crystallinity before and after doping.

In order to further verify the existence of $\{Mo_{132}\}$ in the composite material and the chemical state of each element in the composite material, we conducted the X-ray energy spectrum (EDX) (Fig. S3, ESI†) and X-ray photoelectron spectroscopy (XPS) tests (Fig. 4 and Fig. S4, ESI†). Fig. S3 (ESI†) proves that $\{Mo_{132}\}$ is uniformly distributed in the SnO_2 ETL. For SnO_2, Sn 3d shows binding energies at 487.1 eV and 495.54 eV, while for $SnO_2@Mo_{132}$, Sn 3d shows binding energies at 486.5 eV and 494.95 eV. The shifted Sn 3d binding energy demonstrates that there is electron transfer between SnO_2 and Mo_{132}, rather than a simple physical mixing.[80,81] This is consistent with the results

Fig. 2 (a) Infrared spectrum of SnO_2 and $SnO_2@Mo_{132}$; (b) XRD spectrum of SnO_2 and $SnO_2@Mo_{132}$; (c) top SEM image of SnO_2; (d) top SEM image of $SnO_2@Mo_{132}$; (e) ultraviolet-visible spectrum of SnO_2 and $SnO_2@Mo_{132}$.
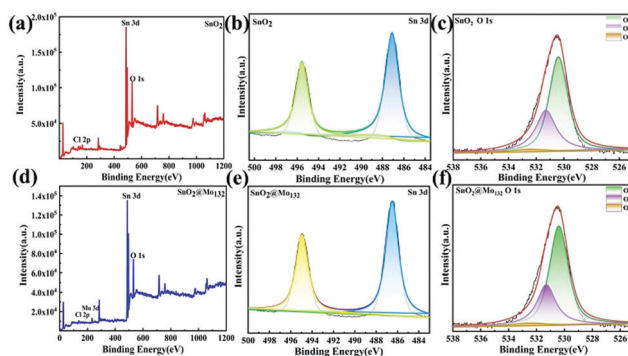
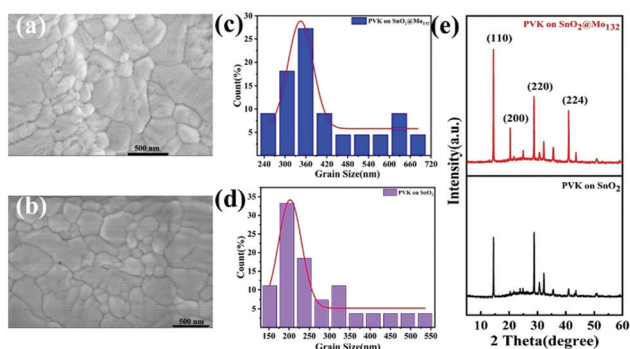Fig. 4 (a)–(c) XPS spectrum of SnO_2; (d)–(f) XPS spectrum of $SnO_2@Mo_{132}$.

of the IR test. O 1s shows binding energy at 530.4 eV (O_1), 531.3 eV (O_2) and 532.5 eV (O_3), respectively. The low binding energy of 530.4 eV is ascribed to the O in the Sn–O bond, and the high binding energy of 531.3 eV and 532.5 eV are attributed to the oxygen vacancies (V_O) and the dangling –OH on the surface of SnO_2.[82–84] We calculated lattice oxygen atoms ($O_{lattice}$) and vacant oxygen atoms (O_{defect}) according to the area of each part under the O 1s curve, as shown in Table S1 (ESI†). It is found that the [$O_{defect}/O_{lattice}$] of $SnO_2@Mo_{132}$ is smaller than that of SnO_2, which indicates that the surface oxygen defects of the doped film are reduced. Schematic illustration of the doped system of the composite is shown in Fig. S5 (ESI†). Surface –OH groups and V_O defects may become charge recombination centers that hinder carrier transport, thereby negatively affecting device performance. Therefore, reduced oxygen defects can also help improve device performance. The binding energies of $Mo_{5/2}$ and $Mo_{3/2}$ in the high binding energy region are 232.3 eV and 235.4 eV, respectively, which are characteristic peaks of fully oxidized Mo^{IV} atoms. The binding energies of $Mo_{5/2}$ and $Mo_{3/2}$ in the low binding energy region are 231.6 eV and 234.4 eV, respectively, which belong to the characteristic peaks of Mo^V atoms in the reduced state.[85,86]

We performed UV-vis spectroscopy (UV-vis) tests on SnO_2 and $SnO_2@Mo_{132}$ to study their optical properties, as shown in Fig. 2e. Compared with pure SnO_2, the absorption of composite $SnO_2@Mo_{132}$ in the entire ultraviolet and visible light region can significantly improve, which shows that the doping of {Mo_{132}} improves the UV-visible light absorption of the composite material, which can also further increase the photocurrent of the device.

3.2 Characterization of perovskite films

As we all know, the quality of perovskite films determines the performance of perovskite-based devices. Therefore, we performed scanning electron microscopy (SEM) and X-ray diffraction spectroscopy (XRD) tests on the perovskite layer, as shown in Fig. 5.

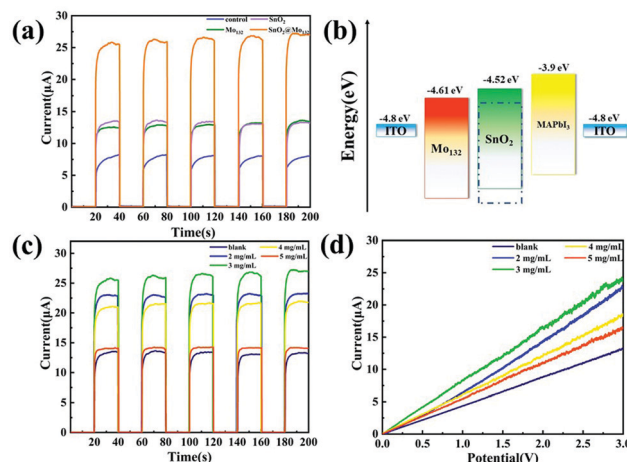It can be seen from the top scanning electron micrograph that the perovskite layers grown on SnO_2 and $SnO_2@Mo_{132}$ are dense and have relatively high crystallinity, which can be further confirmed by XRD patterns. We counted the grain size of perovskite layer, and analyzed the data with a Gaussian curve, as shown in Fig. 5c and d. Compared with the control film, the average grain size of the film grown on $SnO_2@Mo_{132}$ increased from 246.61 nm to 393.74 nm, which indicates that the rich COO^- ligands in {Mo_{132}} can promote the growth of the perovskite layer.[87,88]

The XRD pattern shows that the crystallinity of the perovskite layer is very high. There are two sharp diffraction peaks at 14.45° and 28.75°, corresponding to the (110) and (220) crystal planes of the perovskite, respectively. The perovskite film grown on $SnO_2@Mo_{132}$ has a significantly enhanced diffraction peak intensity on the (110), (200) and (224) crystal plane, indicating that the perovskite film grown on $SnO_2@Mo_{132}$ has higher crystallinity.

3.3 Characterization of device performance

To explore the influence of {Mo_{132}} doping on device performance, we characterized the device performance of SnO_2, Mo_{132} and $SnO_2@Mo_{132}$, respectively, and the corresponding results are shown in Fig. 6a. The figure shows that the photocurrent has high reproducibility after multiple light switches, indicating that the stability of this perovskite-based photodetector is very good. The performance improvement of the device with {Mo_{132}} can be attributed to the excellent optical activity of {Mo_{132}}, which acts as an electron donor/acceptor under light to accelerate electron transport. The photocurrent of the device with the composite material used as the ETL is significantly increased. On the one hand, the crystallinity of doped SnO_2 has been improved, which has been confirmed by XRD tests. The improvement of crystallinity is beneficial to the improvement of device performance. On the other hand, the energy levels of each part in the device are shown

Fig. 5 (a) Top SEM image of the perovskite film grown on $SnO_2@Mo_{132}$; (b) top SEM image of the perovskite film grown on SnO_2; (c) grain size graph of the perovskite film grown on $SnO_2@Mo_{132}$; (d) grain size graph of the perovskite film grown on SnO_2; (e) XRD.

Fig. 6 (a) Time-resolved current curves of perovskite photodetectors with different materials as electron transport layers; (b) energy band alignment diagram of the perovskite-based devices (the dotted line represents the $SnO_2@Mo_{132}$). (c) Time-resolved current curve of perovskite-based photodetectors doped with different concentrations of Mo_{132}; (d) linear sweep voltammetry curves of Mo_{132} doped devices with different concentrations.

in Fig. 6b.[89,90] The electronic structural properties of these ETLs are investigated by UV-visible spectrum (UV-vis) and UV photo-electron spectrum (UPS) measurements, as shown in the Fig. S7 (ESI†). The energy levels of SnO_2 and $SnO_2@Mo_{132}$ can be investigated by ultraviolet-visible spectroscopy to be 3.69 eV and 3.55 eV, respectively. The VB of SnO_2 and $SnO_2@Mo_{132}$ can be obtained through the UPS spectrum. VB = $h\nu - (E_{cutoff} - E_{VB})$, where E_{cutoff} is the high binding energy, E_{VB} is the valence band, $h\nu$ = 21.22 eV.[91] The VB energy levels of pristine SnO_2 and $SnO_2@Mo_{132}$ films lay at -8.21 and -8.18 eV, and the corresponding CB energy levels lay at -4.52 and -4.63 eV, respectively. The Mott–Schottky tests (Fig. S8, ESI†) also confirmed that with the addition of polyoxometalate, the flat band potential of SnO_2 moved down, which means that the E_{CB} of SnO_2 moved down.[92] The reduction of the energy level can promote the transmission of electrons from the perovskite layer to the SnO_2 layer, thereby promoting the increase of current. At the same time, the COO^- ligands in $\{Mo_{132}\}$ can promote the formation of larger-sized grains of perovskite,[87,88] which can also effectively increase the photocurrent of the perovskite-based photodetector. In order to determine the optimal doping amount of polyoxometalate $\{Mo_{132}\}$, we prepared a series of devices with different doping concentrations and tested the time-resolved photocurrent of the device as well as the corresponding I–V curve under simulated AM 1.5 illumination and 3 V bias, as shown in Fig. 6c and d. The time-resolved current curve shows that the optimal doping concentration of $\{Mo_{132}\}$ is 3 mg mL^{-1}, and the corresponding photocurrent can increase from $\sim$13.32 µA to $\sim$27.04 µA. Interestingly, the performance of the device decreases as the concentration of polyoxometalate increases. This is attributed that the characteristic of large-size clustered Kepler polyoxometalate $\{Mo_{132}\}$ that tend to aggregate and cause the coagulation of the SnO_2 colloidal precursor solution when the polyoxometalate concentration increases, thereby reducing the conductivity of SnO_2.[93] The I–V curve corresponding to the time-resolved current curve also shows that when the doping concentration of the polyoxometalate is 3 mg mL^{-1}, the performance of the device is the best. Under the same light intensity, the photocurrent shows an upward trend with the increase of the bias voltage, because the bias voltage can provide power for the migration of electrons. The magnitude of the photocurrent is mainly reflected in the slope of the curve. The larger the slope of the curve, the higher the corresponding photocurrent.

Fig. S9 (ESI†) is the distensible view of time-dependent photocurrent. The rise time t_r (the time it takes for the photocurrent to rise from 10% to 90%) and the fall time t_d (the time it takes for the photocurrent to decay from 90% to 10%) are recorded respectively.[94] The figure shows that, compared with the control device, the t_r of the device after doping with polyoxometalate is significantly shortened, which indicates that the doping of Mo_{132} can effectively inhibit the recombination of electrons and holes existing at the contact interface of perovskite and SnO_2.

To verify the relationship between photocurrent and incident light intensity, we changed the light intensity (80 mW cm^{-2}, 100 mW cm^{-2}, 120 mW cm^{-2}, 140 mW cm^{-2}, 160 mW cm^{-2}) to test the photocurrent and I–V curve of the device under
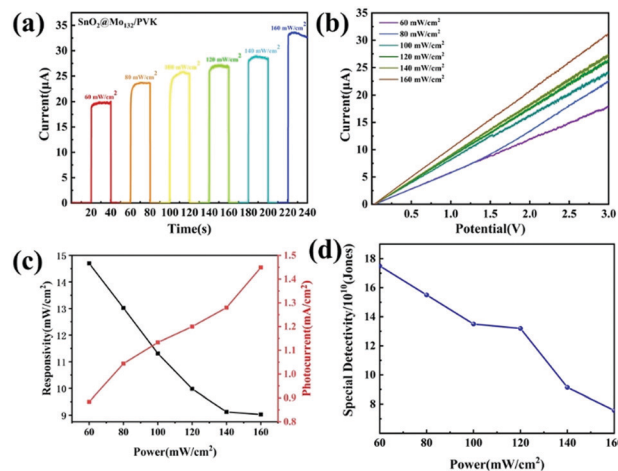

Fig. 7 (a) Time-resolved current curve of a perovskite-based photo-detector on a SnO_2 layer doped with 3 mg mL^{-1} $\{Mo_{132}\}$ under different light intensities; (b) corresponding I–V curve; (c) photocurrent and responsivity of the optimal photodectector under various power intensities; (d) special detectivity (D^*) of the optimal photodectector under various power intensities.

the optimal doping concentration of 3 mg mL^{-1} (Fig. 7 and Fig. S10, ESI†).

The figure reveals that the intensity of incident light is directly proportional to the magnitude of the photocurrent. The increase in photon flux produces more photo-generated electrons as the intensity of incident light increases, thereby increasing the photocurrent of the device. The I–V curve shows that the photocurrent is also proportional to the bias voltage because the bias voltage can provide power for the migration of electrons. Responsivity (R) and the special detectivity (D^*) are important parameters to measure the performance of photodetectors. Photoresponsivity (R) can be defined as the photocurrent generated upon incident light density, which can be calculated according to the following expression:

$$R = \frac{I_p - I_d}{P_{light} \times S} \quad (1)$$

where I_p means photocurrent, I_d is dark current, P_{light} is incident light intensity in the experiment, S is the active area. We drew the photoresponsivity curve under different light power, as shown in Fig. 7c. It can be seen from the figure that as the light power increases, the value of R gradually decreases, which is consistent with previous reports.

The specific detectivity (D^*) is an important parameter of photodetectors, which represents the ability of photodetectors to detect weak light signals, which can be calculated according to the following expression:

$$D^* = \sqrt{\frac{S}{2qI_{dark}}} \quad (2)$$

where I_{dark} is the current in the dark, S is the effective area of the photodetector under illumination, and q is the electron charge.[95] The calculation result is shown in Fig. 7d.
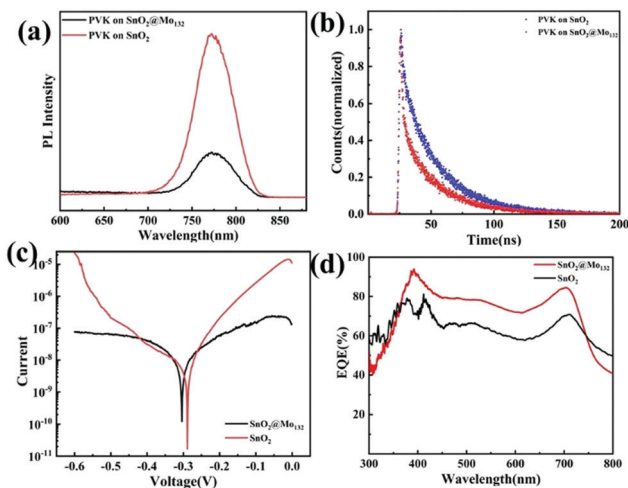
Fig. 8 (a) PL, (b) TRPL decay curves of perovskite films (MAPbI$_3$) with/without {Mo$_{132}$} doping; (c) J–V curves (dark/light); (d) EQE curves of the perovskite photodetectors with/without {Mo$_{132}$} doping at zero bias.

In order to further verify that {Mo$_{132}$} is the most suitable doping material in Kepler-type polyoxometalates, we synthesized a series of Kepler-type polyoxometalates {Mo$_{154}$}, {Mo$_{176}$}, {Mo$_{72}$Cr$_{30}$} and {Mo$_{72}$Fe$_{30}$}, and doped them into SnO$_2$ at a concentration of 3 mg mL^{-1}. The corresponding time-resolved current curve of the device is shown in Fig. S11 (ESI†). It can be seen from the figure that the performance of Kepler-type polyoxometalate-doped devices has generally improved, and the performance of {Mo$_{132}$}-doped devices is the best. Therefore, {Mo$_{132}$} with an inorganic fullerene structure is the best polyoxometalate for doping modification of SnO$_2$.

In order to study the interface electron transport between the perovskite layer and the SnO$_2$ layer, we conducted photoluminescence (PL), time-resolved photoluminescence (TRPL) and SCLC tests, as shown in Fig. 8. The PL spectra of the perovskite layer spin-coated on different ETL layers are presented in Fig. 8a. Compared with the ITO/SnO$_2$/perovskite sample, ITO/SnO$_2$@Mo$_{132}$/perovskite can observe more obvious PL quenching. This shows that photo-generated electrons can be transported to ETL more efficiently.[96] Fig. 8b shows that the fluorescence lifetime of the perovskite layer on SnO$_2$@Mo$_{132}$ is shorter, which indicates that there is less carrier recombination at the interface of the perovskite and SnO$_2$@Mo$_{132}$, and the charge extraction at the interface is faster. This is consistent with a previous study,[96] and the results measured by PL. The SCLC curve is shown as Fig. 8. The dark current density of the photodetector processed by SnO$_2$@Mo$_{132}$ is lower than that of the pristine one. The result further proves that defect passivation toward under-coordinated Pb ions can effectively suppress dark current.[25]

EQE is a vital parameter to measure the photoelectric conversion capability of a photodetector. We tested the EQE of the devices before and after doping {Mo$_{132}$}, as shown in Fig. 8. It can be seen from the figure that after doping {Mo$_{132}$}, the EQE of the device has improved, which can be attributed to the increase in the electron transmission speed between the perovskite layer and the SnO$_2$ layer.[25]

The stability test of the device is shown in Fig. S12 (ESI†). The doped device was tested for thermal stability at 85 °C, and it was found that the device could maintain 65% of the initial current after 70 h. The long-term stability of the device was tested in an ambient environment with an RH condition of 45 ± 5% without encapsulation, and it was found that after 200 h, the device can maintain 70% of the initial current with good stability. Signal stability was performed with a Gamry electrochemical workstation under a broadband noise generator (frequency = 0.05–8 kHz, peak = 1.5 kHz). The noise current is tested at 65 dB, 75 dB and 85 dB respectively. It can be seen from the figure that the current value of the device is relatively stable regardless of whether it is under light or dark conditions (Fig. S13, ESI†).

4. Conclusions

In total, we used simple doping methods to obtain the composite SnO$_2$@Mo$_{132}$ and applied it to the ETL of the perovskite-based photodetector. The composite material has the following advantages. First, the composite material has a more suitable energy level, so that the photogenerated carriers can be transported more effectively, thereby inhibiting the interface charge recombination. Second, the doping of polyoxometalates can reduce the oxygen vacancies of SnO$_2$ and inhibit the charge recombination on SnO$_2$. Third, the abundant carboxyl ligands in {Mo$_{132}$} can promote the crystallization of the perovskite, thereby increasing the crystallinity of the perovskite layer. Fourth, the ultraviolet-visible light absorption intensity of the composite material is significantly improved because the polyoxometalate has good light absorption. Therefore, by using composite materials as the ETL, the photocurrent of the device has been improved a lot. Under simulated AM 1.5 illumination, the photocurrent of the best device is increased by about 2 times. This work provides a new idea for the application of polyoxometalate-based materials to modify semiconductor materials.

Conflicts of interest

The authors declare no competing interests.

Acknowledgements

References

1 E. Akman and S. Akin, Poly(N,N′-bis-4-butylphenyl-N,N′-bisphenyl)benzidine-Based Interfacial Passivation Strategy Promoting Efficiency and Operational Stability of Perovskite Solar Cells in Regular Architecture, *Adv. Mater.*, 2021, **33**, 2006087.

2 A. Ali, Y. Ahn, K. A. Khawaja, J. H. Kang, Y. J. Park, J. H. Seo and B. Walker, A Simple Cu(II) Polyelectrolyte as a Method to Increase the Work Function of Electrodes and Form Effective p-Type Contacts in Perovskite Solar Cells, *Adv. Funct. Mater.*, 2021, **32**, 2009246.

3 M. Du, X. Zhu, L. Wang, H. Wang, J. Feng, X. Jiang, Y. Cao, Y. Sun, L. Duan, Y. Jiao, K. Wang, X. Ren, Z. Yan, S. Pang and S. Liu, High-Pressure Nitrogen-Extraction and Effective Passivation to Attain Highest Large-Area Perovskite Solar Module Efficiency, *Adv. Mater.*, 2020, **32**, 2004979.

4 T.-S. Su, F. T. Eickemeyer, M. A. Hope, F. Jahanbakhshi, M. Mladenović, J. Li, Z. Zhou, A. Mishra, J.-H. Yum, D. Ren, A. Krishna, O. Ouellette, T.-C. Wei, H. Zhou, H.-H. Huang, M. D. Mensi, K. Sivula, S. M. Zakeeruddin, J. V. Milić, A. Hagfeldt, U. Rothlisberger, L. Emsley, H. Zhang and M. Grätzel, Crown Ether Modulation Enables over 23% Efficient Formamidinium-Based Perovskite Solar Cells, *J. Am. Chem. Soc.*, 2020, **142**, 19980–19991.

5 J. Xi, I. Spanopoulos, K. Bang, J. Xu, H. Dong, Y. Yang, C. D. Malliakas, J. M. Hoffman, M. G. Kanatzidis and Z. Wu, Alternative Organic Spacers for More Efficient Perovskite Solar Cells Containing Ruddlesden–Popper Phases, *J. Am. Chem. Soc.*, 2020, **142**, 19705–19714.

6 R. Xia, X.-X. Gao, Y. Zhang, N. Drigo, V. I. E. Queloz, F. F. Tirani, R. Scopelliti, Z. Huang, X. Fang, S. Kinge, Z. Fei, C. Roldán-Carmona, M. K. Nazeeruddin and P. J. Dyson, An Efficient Approach to Fabricate Air-Stable Perovskite Solar Cells via Addition of a Self-Polymerizing Ionic Liquid, *Adv. Mater.*, 2020, **32**, 2003801.

7 L. Xie, P. Vashishtha, T. M. Koh, P. C. Harikesh, N. F. Jamaludin, A. Bruno, T. J. N. Hooper, J. Li, Y. F. Ng, S. G. Mhaisalkar and N. Mathews, Realizing Reduced Imperfections via Quantum Dots Interdiffusion in High Efficiency Perovskite Solar Cells, *Adv. Mater.*, 2020, **32**, 2003296.

8 Z. Yao, F. Zhang, Y. Guo, H. Wu, L. He, Z. Liu, B. Cai, Y. Guo, C. J. Brett, Y. Li, C. V. Srambickal, X. Yang, G. Chen, J. Widengren, D. Liu, J. M. Gardner, L. Kloo and L. Sun, Conformational and Compositional Tuning of Phenanthrocarbazole-Based Dopant-Free Hole-Transport Polymers Boosting the Performance of Perovskite Solar Cells, *J. Am. Chem. Soc.*, 2020, **142**, 17681–17692.

9 Z. Han, W. Fu, Y. Zou, Y. Gu, J. Liu, B. Huang, D. Yu, F. Cao, X. Li, X. Xu and H. Zeng, Oriented Perovskite Growth Regulation Enables Sensitive Broadband Detection and Imaging of Polarized Photons Covering 300–1050 nm, *Adv. Mater.*, 2021, **32**, 2003852.

10 J.-E. Jeong, J. H. Park, C. H. Jang, M. H. Song and H. Y. Woo, Multifunctional Charge Transporting Materials for Perovskite Light-Emitting Diodes, *Adv. Mater.*, 2020, **32**, 2002176.

11 Y.-H. Kim, H. Cho, J. H. Heo, T.-S. Kim, N. Myoung, C.-L. Lee, S. H. Im and T.-W. Lee, Multicolored Organic/Inorganic Hybrid Perovskite Light-Emitting Diodes, *Adv. Mater.*, 2015, **27**, 1248–1254.

12 Z.-K. Tan, R. S. Moghaddam, M. L. Lai, P. Docampo, R. Higler, F. Deschler, M. Price, A. Sadhanala, L. M. Pazos, D. Credgington, F. Hanusch, T. Bein, H. J. Snaith and R. H. Friend, Bright light-emitting diodes based on organometal halide perovskite, *Nat. Nanotechnol.*, 2014, **9**, 687–692.

13 Z. Xiao, R. A. Kerner, L. Zhao, N. L. Tran, K. M. Lee, T.-W. Koh, G. D. Scholes and B. P. Rand, Efficient perovskite light-emitting diodes featuring nanometre-sized crystallites, *Nat. Photonics*, 2017, **11**, 108–115.

14 G. Xing, N. Mathews, S. S. Lim, N. Yantara, X. Liu, D. Sabba, M. Grätzel, S. Mhaisalkar and T. C. Sum, Low-temperature solution-processed wavelength-tunable perovskites for lasing, *Nat. Mater.*, 2014, **13**, 476–480.

15 H. Zhu, Y. Fu, F. Meng, X. Wu, Z. Gong, Q. Ding, M. V. Gustafsson, M. T. Trinh, S. Jin and X. Y. Zhu, Lead halide perovskite nanowire lasers with low lasing thresholds and high quality factors, *Nat. Mater.*, 2015, **14**, 636–642.

16 D. H. Chun, Y. J. Choi, Y. In, J. K. Nam, Y. J. Choi, S. Yun, W. Kim, D. Choi, D. Kim, H. Shin, J. H. Cho and J. H. Park, Halide Perovskite Nanopillar Photodetector, *ACS Nano*, 2018, **12**, 8564–8571.

17 B. Du, W. Yang, Q. Jiang, H. Shan, D. Luo, B. Li, W. Tang, F. Lin, B. Shen, Q. Gong, X. Zhu, R. Zhu and Z. Fang, Plasmonic-Functionalized Broadband Perovskite Photodetector, *Adv. Opt. Mater.*, 2018, **6**, 1701271.

18 W. Tian, H. Zhou and L. Li, Hybrid Organic–Inorganic Perovskite Photodetectors, *Small*, 2017, **13**, 1702107.

19 L. Zheng, T. Zhu, W. Xu, J. Zheng, L. Liu and X. Gong, Ultrasensitive Perovskite Photodetectors by Co Partially Substituted Hybrid Perovskite, *ACS Sustainable Chem. Eng.*, 2018, **6**, 12055–12060.

20 Z. Zhu, W. Deng, W. Li, F. Chun, C. Luo, M. Xie, B. Pu, N. Lin, B. Gao and W. Yang, Antisolvent-Induced Fastly Grown All-Inorganic Perovskite CsPbCl₃ Microcrystal Films for High-Sensitive UV Photodetectors, *Adv. Mater. Interfaces*, 2021, 2001812.

21 Y. Dong, Y. Zou, J. Song, X. Song and H. Zeng, Recent progress of metal halide perovskite photodetectors, *J. Mater. Chem. C*, 2017, **44**, 11369–11394.

22 X. Huang, J. Du, X. Guo, Z. Lin, J. Ma, J. Su, L. Feng, C. Zhang, J. Zhang, J. Chang and Y. Hao, Polyelectrolyte-Doped SnO₂ as a Tunable Electron Transport Layer for High-Efficiency and Stable Perovskite Solar Cells, *Sol. RRL*, 2020, **1**, 1900336.

23 C. Li, J. Lu, Y. Zhao, L. Sun, G. Wang, Y. Ma, S. Zhang, J. Zhou, L. Shen and W. Huang, Highly Sensitive, Fast Response Perovskite Photodetectors Demonstrated in Weak Light Detection Circuit and Visible Light Communication System, *Small*, 2019, **44**, 1903599.

24 C. Li, H. Wang, F. Wang, T. Li, M. Xu, H. Wang, Z. Wang, X. Zhan, W. Hu and L. Shen, Ultrafast and broadband photodetectors based on a perovskite/organic bulk heterojunction

for large-dynamic-range imaging, *Light: Sci. Appl.*, 2020, **1**, 31.

25 N. Ma, J. Jiang, Y. Zhao, L. He, Y. Ma, H. Wang, L. Zhang, C. Shan, L. Shen and W. Hu, Stable and sensitive tin-lead perovskite photodetectors enabled by azobenzene derivative for near-infrared acousto-optic conversion communications, *Nano Energy*, 2021, 106113.

26 L. Shen, Y. Fang, D. Wang, Y. Bai, Y. Deng, M. Wang, Y. Lu and J. Huang, A Self-Powered, Sub-nanosecond-Response Solution-Processed Hybrid Perovskite Photodetector for Time-Resolved Photoluminescence-Lifetime Detection, *Adv. Mater.*, 2016, **48**, 10794–10800.

27 W. Tian, H. Zhou and L. Li, Hybrid Organic–Inorganic Perovskite Photodetectors, *Small*, 2017, **41**, 1702107.

28 H. Wang and D. H. Kim, Perovskite-based photodetectors: materials and devices, *Chem. Soc. Rev.*, 2017, **17**, 5204–5236.

29 Y. Xiao, C. Zuo, J. X. Zhong, W. Q. Wu, L. Shen and L. Ding, Large-Area Blade-Coated Solar Cells: Advances and Perspectives, *Adv. Energy Mater.*, 2021, **21**, 2100378.

30 Y. Zhao, C. Li, J. Jiang, B. Wang and L. Shen, Sensitive and Stable Tin–Lead Hybrid Perovskite Photodetectors Enabled by Double-Sided Surface Passivation for Infrared Upconversion Detection, *Small*, 2020, **26**, 2001534.

31 Y. Zhao, C. Li and L. Shen, Recent advances on organic-inorganic hybrid perovskite photodetectors with fast response, *InfoMat*, 2019, **2**, 164–182.

32 G. Gao, Q. Xi, H. Zhou, Y. Zhao, C. Wu, L. Wang, P. Guo and J. Xu, Novel inorganic perovskite quantum dots for photo-catalysis, *Nanoscale*, 2017, **9**, 12032–12038.

33 M. Wang, Y. Zuo, J. Wang, Y. Wang, X. Shen, B. Qiu, L. Cai, F. Zhou, S. P. Lau and Y. Chai, Remarkably Enhanced Hydrogen Generation of Organolead Halide Perovskites via Piezocatalysis and Photocatalysis, *Adv. Energy Mater.*, 2019, **9**, 1901801.

34 Z. Zhang, Y. Liang, H. Huang, X. Liu, Q. Li, L. Chen and D. Xu, Stable and Highly Efficient Photocatalysis with Lead-Free Double-Perovskite of $Cs_2AgBiBr_6$, *Angew. Chem., Int. Ed.*, 2019, **58**, 7263–7267.

35 G. C. Xing, S. Y. Sun, S. S. Lim, Y. M. Lam, M. Grätzel, S. Mhaisalkar and T. C. Sum, Long-Range Balanced Electron- and Hole-Transport Lengths in Organic-Inorganic $CH_3NH_3PbI_3$, *Science*, 2013, **342**, 344–347.

36 N. J. Jeon, J. H. Noh, W. S. Yang, Y. C. Kim, S. Ryu, J. Seo and S. I. Seok, Compositional engineering of perovskite materials for high-performance solar cells, *Nature*, 2015, **517**, 476–480.

37 E. J. Juarez-Perez, R. S. Sanchez, L. Badia, G. Garcia-Belmonte, Y. S. Kang, I. Mora-Sero and J. Bisquert, Photo-induced Giant Dielectric Constant in Lead Halide Perovskite Solar Cells, *J. Phys. Chem. Lett.*, 2014, **5**, 2390–2394.

38 H. Wei, Y. Fang, P. Mulligan, W. Chuirazzi, H.-H. Fang, C. Wang, B. R. Ecker, Y. Gao, M. A. Loi, L. Cao and J. Huang, Sensitive X-ray detectors made of methylammonium lead tribromide perovskite single crystals, *Nat. Photonics*, 2016, **10**, 333–339.

39 P. Calado, A. M. Telford, D. Bryant, X. Li, J. Nelson, B. C. O'Regan and P. R. F. Barnes, Evidence for ion migration in hybrid perovskite solar cells with minimal hysteresis, *Nat. Commun.*, 2016, **7**, 13831.

40 C. Li, S. Tscheuschner, F. Paulus, P. E. Hopkinson, J. Kießling, A. Köhler, Y. Vaynzof, S. Huettner and S. Huettner, Iodine Migration and its Effect on Hysteresis in Perovskite Solar Cells, *Adv. Mater.*, 2016, **28**, 2446–2454.

41 D. Yang, X. Zhou, R. Yang, Z. Yang, W. Yu, X. Wang, C. Li, S. Liu and R. P. H. Chang, Surface optimization to eliminate hysteresis for record efficiency planar perovskite solar cells, *Energy Environ. Sci.*, 2016, **9**, 3071–3078.

42 J. You, Z. Hong, Y. Yang, Q. Chen, M. Cai, T.-B. Song, C.-C. Chen, S. Lu, Y. Liu, H. Zhou and Y. Yang, Low-Temperature Solution-Processed Perovskite Solar Cells with High Efficiency and Flexibility, *ACS Nano*, 2014, **8**, 1674–1680.

43 X. Zheng, B. Chen, J. Dai, Y. Fang, Y. Bai, Y. Lin and H. Wei, Xiao C. Zeng and J. Huang, Defect passivation in hybrid perovskite solar cells using quaternary ammonium halide anions and cations, *Nat. Energy*, 2017, **2**, 17102.

44 Y. Wang, J. Wan, J. Ding, J.-S. Hu and D. Wang, A Rutile TiO_2 Electron Transport Layer for the Enhancement of Charge Collection for Efficient Perovskite Solar Cells, *Angew. Chem., Int. Ed.*, 2019, **58**, 9414–9418.

45 J. Cao, X. Lv, P. Zhang, T. T. Chuong, B. Wu, X. Feng and C. Shan, Plant Sunscreen and Co(II)/(III) Porphyrins for UV-Resistant and Thermally Stable Perovskite Solar Cells: From Natural to Artificial, *Adv. Mater.*, 2018, **30**, 1800568.

46 T. Leijtens, G. E. Eperon, S. Pathak, A. Abate, M. M. Lee and H. J. Snaith, Overcoming ultraviolet light instability of sensitized TiO_2 with meso-superstructured organometal tri-halide perovskite solar cells, *Nat. Commun.*, 2013, **4**, 2885.

47 S. Ito, S. Tanaka, K. Manabe and H. Nishino, Effects of Surface Blocking Layer of Sb_2S_3 on Nanocrystalline TiO_2 for $CH_3NH_3PbI_3$ Perovskite Solar Cells, *J. Phys. Chem. C*, 2014, **118**, 16995–17000.

48 Q. Jiang, X. Zhang and J. You, SnO_2: A Wonderful Electron Transport Layer for Perovskite Solar Cells, *Small*, 2018, **14**, 1801154.

49 C. Chen, Y. Jiang, J. Guo, X. Wu, W. Zhang, S. Wu, X. Gao, X. Hu, Q. Wang, G. Zhou, Y. Chen, J.-M. Liu, K. Kempa and J. Gao, Solvent-Assisted Low-Temperature Crystallization of SnO_2 Electron-Transfer Layer for High-Efficiency Planar Perovskite Solar Cells, *Adv. Funct. Mater.*, 2019, **29**, 1900557.

50 S. Song, G. Kang, L. Pyeon, C. Lim, G.-Y. Lee, T. Park and J. Choi, Systematically Optimized Bilayered Electron Transport Layer for Highly Efficient Planar Perovskite Solar Cells (η = 21.1%), *ACS Energy Lett.*, 2017, **2**, 2667–2673.

51 Q. Jiang, L. Zhang, H. Wang, X. Yang, J. Meng, H. Liu, Z. Yin, J. Wu, X. Zhang and J. You, Enhanced electron extraction using SnO_2 for high-efficiency planar-structure $HC(NH_2)_2PbI_3$-based perovskite solar cells, *Nat. Energy*, 2016, **2**, 16177.

52 R. L. Milot, G. E. Eperon, H. J. Snaith, M. B. Johnston and L. M. Herz, Temperature-Dependent Charge-Carrier Dynamics in $CH_3NH_3PbI_3$ Perovskite Thin Films, *Adv. Funct. Mater.*, 2015, **25**, 6218–6227.

53 S. S. Mali, J. V. Patil, H. Kim and C. K. Hong, Synthesis of SnO_2 nanofibers and nanobelts electron transporting layer

for efficient perovskite solar cells, *Nanoscale*, 2018, **10**, 8275–8284.

54 Q. Fu, S. Xiao, X. Tang, Y. Chen and T. Hu, Amphiphilic Fullerenes Employed to Improve the Quality of Perovskite Films and the Stability of Perovskite Solar Cells, *ACS Appl. Mater. Interfaces*, 2019, **27**, 24782–24788.

55 X. Liu, F. Lin, C.-C. Chueh, Q. Chen, T. Zhao, P.-W. Liang, Z. Zhu, Y. Sun and A. K. Y. Jen, Fluoroalkyl-substituted fullerene/perovskite heterojunction for efficient and ambient stable perovskite solar cells, *Nano Energy*, 2016, 417–425.

56 J. Wei, F. Guo, X. Wang, K. Xu, M. Lei, Y. Liang, Y. Zhao and D. Xu, SnO₂-in-Polymer Matrix for High-Efficiency Perovskite Solar Cells with Improved Reproducibility and Stability, *Adv. Mater.*, 2018, **30**, 1805153.

57 W. Hui, Y. Yang, Q. Xu, H. Gu, S. Feng, Z. Su, M. Zhang, J. Wang, X. Li, J. Fang, F. Xia, Y. Xia, Y. Chen, X. Gao and W. Huang, Red-Carbon-Quantum-Dot-Doped SnO₂ Composite with Enhanced Electron Mobility for Efficient and Stable Perovskite Solar Cells, *Adv. Mater.*, 2020, **32**, 1906374.

58 W. Ke, D. Zhao, C. Xiao, C. Wang, A. J. Cimaroli, C. R. Grice, M. Yang, Z. Li, C.-S. Jiang, M. Al-Jassim, K. Zhu, M. G. Kanatzidis, G. Fang and Y. Yan, Cooperative tin oxide fullerene electron selective layers for high-performance planar perovskite solar cells, *J. Mater. Chem. A*, 2016, **4**, 14276–14283.

59 K. Liu, S. Chen, J. Wu, H. Zhang, M. Qin, X. Lu, Y. Tu, Q. Meng and X. Zhan, Fullerene derivative anchored SnO₂ for high-performance perovskite solar cells, *Energy Environ. Sci.*, 2018, **11**, 3463–3471.

60 J. Wang, K. Datta, C. H. L. Weijtens, M. M. Wienk and R. A. J. Janssen, Insights into Fullerene Passivation of SnO₂ Electron Transport Layers in Perovskite Solar Cells, *Adv. Funct. Mater.*, 2019, **29**, 1905883.

61 N. Li, Z. Sun, R. Liu, L. Xu, K. Xu and X.-M. Song, Enhanced power conversion efficiency in phthalocyanine-sensitized solar cells by modifying TiO₂ photoanode with polyoxometalate, *Sol. Energy Mater. Sol. Cells*, 2016, **157**, 853–860.

62 J. T. Arens, M. Blasco-Ahicart, K. Azmani, J. Soriano-López, A. García-Eguizábal, J. M. Poblet and J. R. Galan-Mascaros, Water oxidation electrocatalysis in acidic media with Co-containing polyoxometalates, *J. Catal.*, 2020, **389**, 345–351.

63 Z. H. Wang, X. F. Wang, Z. Tan and X. Z. Song, Polyoxometalate/metal–organic framework hybrids and their derivatives for hydrogen and oxygen evolution electrocatalysis, *Mater. Today Energy*, 2021, **19**, 100618.

64 K. Suzuki, N. Mizuno and K. Yamaguchi, Polyoxometalate Photocatalysis for Liquid-Phase Selective Organic Functional Group Transformations, *ACS Catal.*, 2018, **8**, 10809–10825.

65 Y. Li, M. Liu and L. Chen, Polyoxometalate built-in conjugated microporous polymers for visible-light heterogeneous photocatalysis, *J. Mater. Chem. A*, 2017, **5**, 13757–13762.

66 Y. Zhang, R. Tao, X. Zhao, Z. Sun, Y. Wang and L. Xu, A highly photoconductive composite prepared by incorporating polyoxometalate into perovskite for photodetection application, *Chem. Commun.*, 2016, **52**, 3304–3307.

67 M. K. Sardashti, M. Zendehdel, N. Y. Nia, D. Karimian and M. Sheikhi, High Efficiency MAPbI₃ Perovskite Solar Cell Using a Pure Thin Film of Polyoxometalate as Scaffold Layer, *ChemSusChem*, 2017, **10**, 3773–3779.

68 Q. Wang, J. Khungwa, L. Li, Y. Liu, X. Wang and S. Wang, Fabrication of polyoxometalate/GO/PDDA hybrid nano-composite modified electrode and electrocatalysis for nitrite ion, ascorbic acid and dopamine, *J. Electroanal. Chem.*, 2018, **824**, 91–98.

69 J. Ran, L. Xiao, W. Wang, S. Jia and J. Zhang, Correction: ZIF-8@polyoxometalate derived Si-doped ZnWO₄@ZnO nanocapsules with open-shaped structures for efficient visible light photocatalysis, *Chem. Commun.*, 2018, **54**, 13869.

70 X. Fan, J. Zhang, Y. Yang, D. Xia, Y. Dong, L. Qiu, J. Wang, W. Cao, B. Hu, W. Wang and R. Fan, Chemical doping engineering by utilizing trilacunary Keggin polyoxometalates as a dopant for high performance perovskite solar cells, *Dalton Trans.*, 2021, **50**, 279–286.

71 L. Chen, W.-L. Chen, X.-L. Wang, Y.-G. Li, Z.-M. Su and E.-B. Wang, Polyoxometalates in dye-sensitized solar cells, *Chem. Soc. Rev.*, 2019, **48**, 260–284.

72 L. Chen, W. L. Chen, X. L. Wang, Y. G. Li, Z. M. Su, E. B. Wang and Z. H. Kang, Keplerate-type polyoxometalate/semiconductor composite electrodes with light-enhanced conductivity towards highly efficient photoelectronic devices, *J. Mater. Chem. A*, 2016, **4**, 14025–14032.

73 L. Guan, N. Jiao and Y. Guo, Trap-State Passivation by Nonvolatile Small Molecules with Carboxylic Acid Groups for Efficient Planar Perovskite Solar Cells, *J. Phys. Chem. C*, 2019, **23**, 14223–14228.

74 L. Zhang, K. Cao, J. Qian, Y. Huang, X. Wang, M. Ge, W. Shen, F. Huang, M. Wang, W. Zhang, S. Chen and T. Qin, Crystallization control and multisite passivation of perovskites with amino acid to boost the efficiency and stability of perovskite solar cells, *J. Mater. Chem. C*, 2020, **48**, 17482–17490.

75 A. Müller, E. Krickemeyer, H. Bögge, M. Schmidtmann and F. Peters, Organizational Forms of Matter: An Inorganic Super Fullerene and Keplerate Based on Molybdenum Oxide, *Angew. Chem., Int. Ed.*, 1998, **37**, 3359–3363.

76 A. Mojaverian Kermani, A. Ahmadpour, T. Rohani Bastami and M. Ghahramaninezhad, Deep oxidative desulfurization of dibenzothiophene with {Mo₁₃₂} nanoballs supported on activated carbon as an efficient catalyst at room temperature, *New J. Chem.*, 2018, **42**, 12188–12197.

77 Y. Ai, W. Liu, C. Shou, J. Yan, N. Li, Z. Yang, W. Song, B. Yan, J. Sheng and J. Ye, SnO₂ surface defects tuned by (NH₄)₂S for high-efficiency perovskite solar cells, *Sol. Energy*, 2019, **194**, 541–547.

78 Z. Zhu, Y. Bai, X. Liu, C.-C. Chueh, S. Yang and A. K. Y. Jen, Enhanced Efficiency and Stability of Inverted Perovskite Solar Cells Using Highly Crystalline SnO₂ Nanocrystals as the Robust Electron-Transporting Layer, *Adv. Mater.*, 2016, **28**, 6478–6484.

79 E. Jiang, Y. Ai, J. Yan, N. Li, L. Lin, Z. Wang, C. Shou, B. Yan, Y. Zeng, J. Sheng and J. Ye, Phosphate-Passivated SnO₂ Electron Transport Layer for High-Performance Perovskite Solar Cells, *ACS Appl. Mater. Interfaces*, 2019, **11**, 36727–36734.

80 Y. H. Kim, D. G. Kim, R. D. Maduwu, H. C. Jin, D. K. Moon and J. H. Kim, Organic Electrolytes Doped ZnO Layer as the Electron Transport Layer for Bulk Heterojunction Polymer Solar Cells, *Sol. RRL*, 2018, **2**, 1800086.

81 R. Tao, Y. Zhang, Z. Jin, Z. Sun and L. Xu, Polyoxometalate doped tin oxide as electron transport layer for low cost, hole-transport-material-free perovskite solar cells, *Electrochim. Acta*, 2018, **284**, 10–17.

82 X. Wang, Q. Di, X. Wang, H. Zhao, B. Liang and J. Yang, Effect of oxygen vacancies on photoluminescence and electrical properties of (200) oriented fluorine-doped SnO_2 films, *Mater. Sci. Eng., B*, 2019, **250**, 114433.

83 H. B. Lee, N. Kumar, M. M. Ovhal, Y. J. Kim, Y. M. Song and J.-W. Kang, Dopant-Free, Amorphous–Crystalline Heterophase SnO_2 Electron Transport Bilayer Enables >20% Efficiency in Triple-Cation Perovskite Solar Cells, *Adv. Funct. Mater.*, 2020, **30**, 2001559.

84 H. B. Lee, R. T. Ginting, S. T. Tan, C. H. Tan, A. Alshanableh, H. F. Oleiwi, C. C. Yap, M. H. H. Jumali and M. Yahaya, Controlled Defects of Fluorine-incorporated ZnO Nanorods for Photovoltaic Enhancement, *Sci. Rep.*, 2016, **6**, 32645.

85 M. Vasilopoulou, A. M. Douvas, L. C. Palilis, S. Kennou and P. Argitis, Old Metal Oxide Clusters in New Applications: Spontaneous Reduction of Keggin and Dawson Polyoxometalate Layers by a Metallic Electrode for Improving Efficiency in Organic Optoelectronics, *J. Am. Chem. Soc.*, 2015, **137**, 6844–6856.

86 M. Vasilopoulou, A. M. Douvas, D. G. Georgiadou, L. C. Palilis, S. Kennou, L. Sygellou, A. Soultati, I. Kostis, G. Papadimitropoulos, D. Davazoglou and P. Argitis, The Influence of Hydrogenation and Oxygen Vacancies on Molybdenum Oxides Work Function and Gap States for Application in Organic Optoelectronics, *J. Am. Chem. Soc.*, 2012, **134**, 16178–16187.

87 J. Peng, J. I. Khan, W. Liu, E. Ugur, T. Duong, Y. Wu, H. Shen, K. Wang, H. Dang, E. Aydin, X. Yang, Y. Wan, K. J. Weber, K. R. Catchpole, F. Laquai, S. De Wolf and T. P. White, A Universal Double-Side Passivation for High Open-Circuit Voltage in Perovskite Solar Cells: Role of Carbonyl Groups in Poly(methyl methacrylate), *Adv. Energy Mater.*, 2018, **8**, 1801208.

88 Z. Liu, F. Cao, M. Wang, M. Wang and L. Li, Observing Defect Passivation of the Grain Boundary with 2-Amino-terephthalic Acid for Efficient and Stable Perovskite Solar Cells, *Angew. Chem., Int. Ed.*, 2020, **59**, 4161–4167.

89 C. Bo and P. Miró, On the electronic structure of giant polyoxometalates: Mo_{132} vs. $W_{72}Mo_{60}$, *Dalton Trans.*, 2012, **41**, 9984–9988.

90 A. K. Jena, A. Kulkarni and T. Miyasaka, Halide Perovskite Photovoltaics: Background, Status, and Future Prospects, *Chem. Rev.*, 2019, **119**, 3036–3103.

91 L. Zhang, K. Cao, J. Qian, Y. Huang, X. Wang, M. Ge, W. Shen, F. Huang, M. Wang, W. Zhang, S. Chen and T. Qin, Crystallization control and multisite passivation of perovskites with amino acid to boost the efficiency and stability of perovskite solar cells, *J. Mater. Chem. C*, 2020, **48**, 17482–17490.

92 C. Huang, C. Liu, Y. Di, W. Li, F. Liu, L. Jiang, J. Li, X. Hao and H. Huang, Efficient Planar Perovskite Solar Cells with Reduced Hysteresis and Enhanced Open Circuit Voltage by Using PW_{12}–TiO_2 as Electron Transport Layer, *ACS Appl. Mater. Interfaces*, 2016, **8**, 8520–8526.

93 M. L. Kistler, A. Bhatt, G. Liu, D. Casa and T. Liu, A Complete Macroion−"Blackberry" Assembly−Macroion Transition with Continuously Adjustable Assembly Sizes in {Mo_{132}} Water/Acetone Systems, *J. Am. Chem. Soc.*, 2007, **129**, 6453–6460.

94 S. Du, G. Li, X. Cao, Y. Wang, H. Lu, S. Zhang, C. Liu and H. Zhou, Oxide Semiconductor Phototransistor with Organolead Trihalide Perovskite Light Absorber, *Adv. Electron. Mater.*, 2017, **4**, 1600325.

95 J. Xu, H. Wang, S. Yang, G. Ni and B. Zou, High-sensitivity broadband colloidal quantum dot heterojunction photodetector for night-sky radiation, *J. Alloys Compd.*, 2018, 446–451.

96 H. Zhao, J. Xu, Y. Yang, Z. Li, B. Zhang, X. Liu, S. Dai and J. Yao, Enhancement of the Interfacial Connection via Carboxyl-Substituted Perylene as Electron-Transport Layer for Efficient and Stable Perovskite Solar Cells, *Sol. RRL*, 2018, **11**, 1800205.